Nanoscale

Accepted Manuscript

This article can be cited before page numbers have been issued, to do this please use: B. Peng, J. Cui, Y. Wang, J. Liu, H. Zheng, L. Jin, X. zhang, Y. Zhang and Y. Wu, *Nanoscale*, 2017, DOI: 10.1039/C7NR08858B.

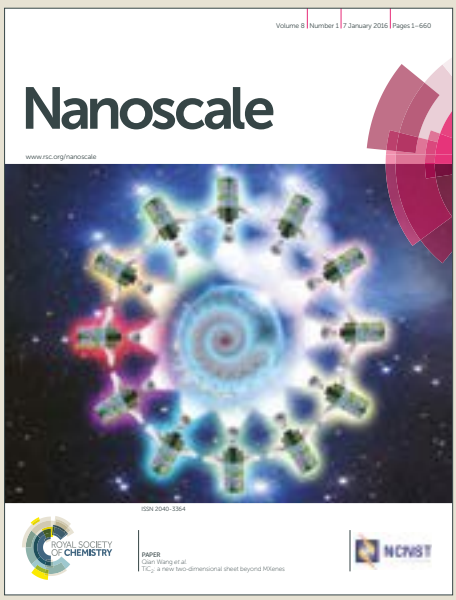

ROYAL SOCIETY OF CHEMISTRY

rsc.li/nanoscale

View Article Online
DOI: 10.1039/C7NR08858B

Journal Name

ARTICLE

CeO_{2-x}/C/rGO nanocomposites derived from Ce-MOF and graphene oxide as robust platform for highly sensitive uric acid detection

Received 00th January 20xx,
Accepted 00th January 20xx

DOI: 10.1039/x0xx00000x

www.rsc.org/

Bangguo Peng[a], Jiewu Cui[a,b,*], Yan Wang [a,b,*], Jiaqin Liu[b], Hongmei Zheng[a,b], Li Jin[a], Xinyi Zhang[c], Yong Zhang[a,b], Yucheng Wu[a,b,*]

Developing suitable substrate materials is of significance in constructing electrochemical biosensors for fast and reliable quantification of chemical and biomedical interest. For practical applications, biosensor working at less negative potentials has the advantage of high selectivity and sensitivity. In this work, CeO_{2-x}/C/rGO nanocomposites have been synthesized through the pyrolysis of metal organic frameworks with graphene oxide. The CeO_{2-x}/C/rGO nanocomposites exhibit excellent catalytic properties towards H_2O_2, which is one of uricase catalyzed intermediates at low working potentials due to the coexistence of Ce^{3+} and reduced graphene oxide (rGO). A novel biosensor based on the CeO_{2-x}/C/rGO nanocomposites has been developed and utilized for the detection of uric acid, an important molecule in biological and medical field. The biosensor based on CeO_{2-x}/C/rGO nanocomposites presents a high sensitivity of 284.5 $\mu A \cdot cm^{-2} \cdot mM^{-1}$ at -0.4 V (*vs.* SCE), a wide linear range between 49.8 and 1050.0 μM and a low detection limit of 2.0 μM. Moreover, it is found that the amperometric responses are free from interference of ascorbic acid and urea, which shows the great potential for practical applications.

Introduction

Electrochemical biosensors have played a significant role in clinic diagnosis, food quality analysis and environmental pollution monitoring in the past decade.[1-4] In terms of analytes in human fluids, numerous electrochemical biosensors have been developed and employed for detecting the concentrations of glucose[5-7], cholesterol[8,9] and uric acid[10,11], which can monitor the health status of human beings. According to most of the literatures on glucose, cholesterol and uric acid biosensors, the sensing mechanism is generally ascribed to the detection of enzymatically catalyzed intermediates, H_2O_2, reflecting the concentration of analytes indirectly[6,12-15]. Undoubtedly, substrate materials used for the construction of electrochemical biosensors are crucial to change the work conditions and improve the performance of as-prepared biosensors, such as working potential, sensitivity, selectivity, linear range etc. And various nanomaterials with large specific surface area and benign biocompatibility have been regarded as superior substrates for producing electrochemical biosensors. Noble metal nanomaterials, such as Pt[16], Au[17] and Ag[8] are extensively employed as substrate to fabricate electrochemical biosensors. However, high cost and scarcity of noble metal nanomaterials impede their applications in the construction of electrochemical biosensors. In addition, electrochemical biosensors based on noble metal nanomaterials usually work at high potentials, not only enzymatically catalyzed intermediates (H_2O_2), but interferences coexisting with analytes are easily oxidized by noble metal nanomaterials, leading to poor selectivity of electrochemical biosensors. Therefore, developing cost effective substrate materials for the electrochemical biosensors that can work at less negative potentials is still a challenge and urgent to be resolved.

Varieties of metal oxide nanomaterials with low cost and abundance have been utilized to fabricate electrochemical biosensor replacing noble metal nanomaterials, such as ZnO[18], Fe_2O_3[19], MnO_x[20], CeO_2[21]. Among various metal oxide nanomaterials, CeO_2 has attracted more and more attention due to its facile oxygen vacancy formation property, excellent biocompatibility, and natural abundance[22-24]. Furthermore, the high isoelectric point of CeO_2 (IEP ~9.2) at pH 7.0 makes the surface of CeO_2 positively charged [25], which is beneficial to bind negatively

[a] *School of Materials Science and Engineering, Hefei University of Technology, Hefei, 230009, China. Emails: jwcui@hfut.edu.cn, stone@hfut.edu.cn, ycwu@hfut.edu.cn*
[b] *Key Laboratory of Advanced Functional Materials and Devices of Anhui Province, Hefei, 230009, China*
[c] *School of Chemistry, Monash University, Clayton, VIC 3800, Australia*
Electronic Supplementary Information (ESI) available:. See DOI: 10.1039/x0xx00000x

View Article Online
DOI: 10.1039/C7NR08858B

charged enzymes with low IEP, such as glucose oxidase (~4.8)[26], cholesterol oxidase(~4.7)[27], uricase (~4.6)[28].

Ansari et al. [25] synthesized nanoporous CeO_2 film by sol-gel method and used it as the substrate to fabricate cholesterol biosensors, which exhibited high sensitivity and wide linear range at working potential of 0.4 V. Subsequently, Patil and his colleagues [21] employed CeO_2 nanorods as the substrate to construct glucose biosensor and it also showed wide linear range between 2 and 26 M with the working potential of 0.8 V. The sensing mechanism of both aforementioned cholesterol and glucose biosensors based on CeO_2 was oxidation of H_2O_2 by Ce^{4+} in CeO_2 at high potentials. However, interferences coexisting with analytes were still prone to be oxidized by Ce^{4+} and resulted in inauthentic signals in the process of measurements. In order to improve the selectivity of as-prepared biosensors, an effective approach is to decrease the working potentials. One of the most important features of CeO_2 is the redox properties between Ce^{3+} and Ce^{4+} due to the formation of oxygen vacancies. High concentration of Ce^{3+} in CeO_2 can trigger the reduction of H_2O_2 at less negative working potentials, thereby avoiding the oxidation of interferences and improving the selectivity of electrochemical biosensors. Therefore, rational design and synthesis of CeO_2 with extensive oxygen vacancies (denoted as CeO_{2-x}) is crucial in constructing electrochemical biosensors.

On the other hand, graphene, a typical 2D carbon material has been extensively developed as sensing substrate for electrochemical biosensors at less negative potentials owing to its large specific surface area, excellent electrical conductivity and low cost[29]. Therefore, many efforts have been exerted into the incorporation of graphene into metal oxide nanomaterials to construct electrochemical biosensors for enhancing the electron transfer capability and improving the catalytic properties of substrate materials and[30, 31]. As a matter of fact, graphene without functional groups is not soluble in environmental benign solvents, thereby, it has become popular to synthesize nanocomposite in graphene oxide (GO) solutions as precursors, and reduced graphene oxide (rGO) can be finally obtained by chemical reduction or heat treatment at high temperatures[32]. To date, the combination of CeO_2 and graphene (or rGO) employed in the construction of electrochemical biosensors has been more and more popular. Jiang et al. [33] synthesized CeO_2/graphene nanocomposites via one-pot hydrothermal method and they were utilized as substrate to detect uric acid by its oxidation at high working potential. They also found that oxygen vacancy in CeO_2 could decrease the oxidation potential (from 0.482 V to 0.348 V) effectively. Subsequently, Radhakrishnan et al. [34] employed CeO_2/rGO nanocomposites as substrate to immobilized horseradish peroxidise and achieved the detection of trace H_2O_2 at negative potentials, improving the anti-interference ability of H_2O_2 biosensors.

However, there have been no reported work on the combination of CeO_2 and graphene(or rGO) and used for uric acid biosensors working at negative potentials. In this study, we synthesize Ce(1,3,5-BTC)$(H_2O)_6$ (abbreviated as Ce-MOF) in GO solutions and Ce-MOF/GO nanocomposites are formed at room temperature. Catalytic performances of as-prepared samples after different calcinations conditions towards uricase catalyzed intermediate H_2O_2 are investigated and the CeO_{2-x}/C/rGO nanocomposites exhibit superior catalytic property towards H_2O_2 at negative working potentials. And the influence of calcinations temperature on the oxygen vacancy in CeO_2 and specific surface area of CeO_{2-x}/C/rGO nanocomposites is investigated. Meanwhile, catalytic property of CeO_{2-x}/C/rGO nanocomposites towards H_2O_2 detection is studied and optimized. Optimized CeO_{2-x}/C/rGO nanocomposites are employed as a substrate to construct electrochemical biosensor. Owing to the synergistic effect of heteronanostructures, the biosensors exhibit excellent selectivity and sensitivity towards uric acid detection.

Experimental section

Chemicals and reagents

Cerium nitrate ($Ce(NO_3)_3$), 1,3,5-Benzenetricarboxylic acid (1,3,5-BTC), uric acid (UA), ascorbic acid (AA), urea were purchased from Sinopharm Chemical Reagent Co. Ltd (Shanghai, China). Glutaraldehyde (GLA), bovine serum albumin (BSA) and uricase from *Arthrobacter globifomis* (EC 1.7.3.3) were obtained from Sigma (USA). All chemicals were analytical grade and used without further purification. Milli-Q water (18.25 MΩ·cm) was employed to prepare solutions throughout the experiments.

Synthesis of Ce-MOF/GO nanocomposites

Graphene oxide (GO) was synthesized firstly according to modified Hummer's method reported previously.[35] A stock solution of GO with concentration of 4 mg ml^{-1} was prepared and used in the following experiments. Prior to the synthesis of Ce-MOF/GO nanocomposites, GO solution after ultrasonication treatment for 2 h was diluted in Milli-Q water with different concentrations and stirred vigorously. Subsequently, 1,3,5-BTC ethanol solution and $Ce(NO_3)_3$ water solution were added to the diluted GO solution under vigorous stirring in sequence at room temperature and a great amount of brown precipitates formed immediately. Finally, Ce-MOF/GO nanocomposites precipitates were obtained by centrifugation at a speed of 4000 rpm for 5 minutes. As-obtained precipitates were washed with ethanol and Milli-Q water several times to remove residual reactant and dried at 100 ℃ for 12 h. Influence of GO concentration, 1,3,5-BTC concentration and $Ce(NO_3)_3$ concentration and reaction time on the morphology of Ce-MOF/GO nanocomposites were investigated, respectively.

Synthesis of CeO_2 and CeO_{2-x}/C/rGO nanocomposites

Dried Ce-MOF/GO nanocomposites precipitates were grinded into fine powders in a agate mortar. The thermal

View Article Online
DOI: 10.1039/C7NR08858B

gravimetric analysis (TGA) was employed to measure the thermal stability of Ce-MOF/GO nanocomposites powders. On the basis of TGA results in Fig.S1, Ce-MOF/GO nanocomposites powders were calcinated at 450 °C in air atmosphere for 2 h and 600 °C in Ar atmosphere with heating rate of 2 °C /min, respectively. During this process, yellow powders and black powders were obtained in Air and Ar atmosphere, respectively. In addition, Ce-MOF/GO nanocomposites powders were also calcinated at 450 °C in Ar atmosphere and the electrochemical properties of as-prepared samples were investigated as control experiment.

Fabrication of uric acid biosensors

Firstly, as-synthesized powders were dispersed in Milli-Q water with ultrasonication for 30 min and then aforementioned dispersed solution with different volume was cast onto glassy carbon electrode to optimize loading amount of CeO_{2-x}/C/rGO nanocomposites towards detection of uricase-catalyzed intermediate, H_2O_2. Subsequently, 10 µl of 100 U mL^{-1} uricase was dropped onto CeO_{2-x}/C/rGO nanocomposites modified glassy carbon electrode with optimized loading amount. During this process, negatively charged uricase was adsorbed on the surface of positively charged CeO_{2-x}. In order to avoid the leakage of uricase and CeO_{2-x}/C/rGO nanocomposites, a 2 µl aliquot of solution containing 2.5 % (w/v) bovine serum albumin (BSA) and 2.8 % (v/v) glutaraldehyde (GLA) was cast onto modified glassy carbon electrode to form a protective film. Enzyme electrode was stored in 0.05 M PBS (pH 7.0) when not in used.

Materials characterization and electrochemical measurements

The morphologies of Ce-MOF/GO, CeO_{2-x}/C/rGO nanocomposites, CeO_2 and other samples were characterized by field emission scanning electron microscopy (FESEM, SU8020, Hitachi, Japan). The microstructure and chemical states of as-prepared samples were investigated by X-ray diffractometer (XRD, D/MAX2500V, Rigaku, Japan), Raman spectroscopy (HR Evolution, Horiba, Jobin Yvon, France), X-ray photoelectron spectroscopy (XPS, Escalab250Xi, Thermo, USA) and TEM (JEM-2100F, JEOL, Japan), respectively. Thermal stability of Ce-MOF/GO nanocomposites was carried out in a Simultaneous Thermal Analyzer (STA, 449F3, Netzsch, Germany). Electrochemical measurements, such as cyclic voltammograms (CV), chronoamperometry were performed in a conventional three electrode system on an Autolab PGSTAT 302N (Metrohm, Switzerland) electrochemical workstation. Enzyme electrode, Pt electrode and saturated calomel electrode (SCE) were used as working electrode, counter electrode and reference electrode, respectively. Cyclic voltammograms of CeO_{2-x}/C/rGO nanocomposites were carried out in 0.05 M PBS (pH 7.0) at scan rate of 10 mV s^{-1}. And chronoamperometry was performed in 0.05 M PBS and recorded with an interval of 0.1 s. All the electrochemical measurements were carried out at room temperature.

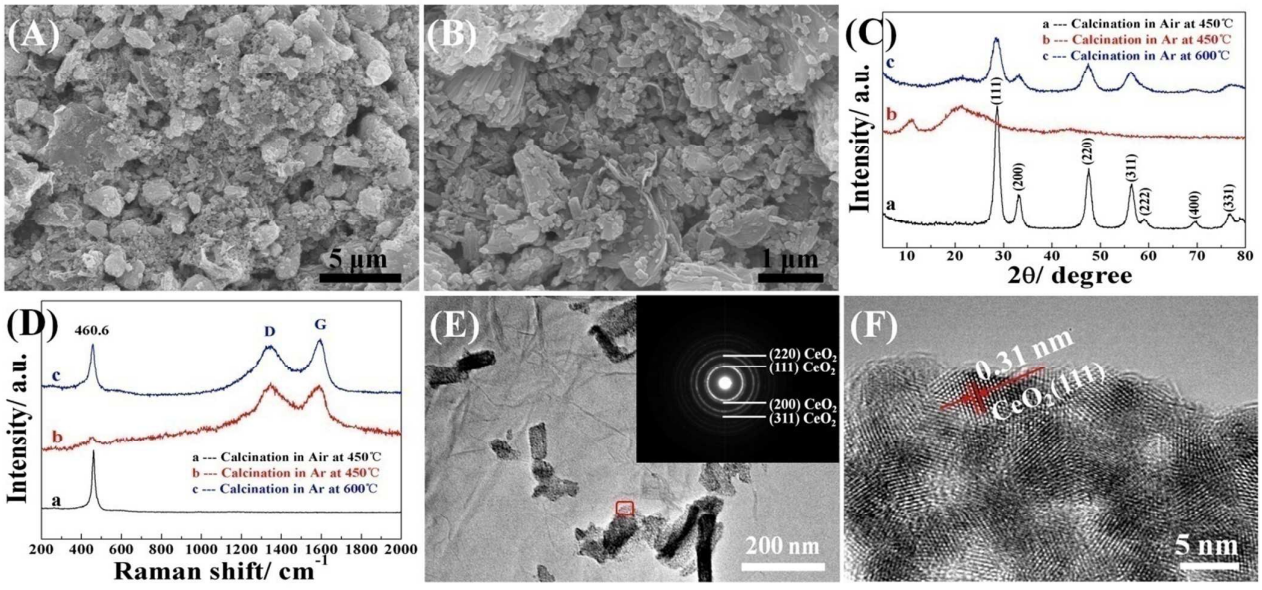

Fig. 1 SEM images of Ce-MOF/GO nanocomposites calcinated at 600℃ in Ar atmosphere with low (A) and high (B) magnifications. (C) and (D) are XRD patterns and Raman spectra of Ce-MOF/GO nanocomposites after different calcination treatment. (E) TEM image of Ce-MOF/GO nanocomposites calcinated at 600 ℃ in Ar atmosphere, inset is the corresponding SAED pattern. (F) HRTEM image of the sample shown in Fig. 1(E).

View Article Online
DOI: 10.1039/C7NR08858B

Journal Name

ARTICLE

Results and discussion

Fig. S2 shows the XRD patterns of as-prepared samples with different conditions. Undoubtedly, Ce-MOF is synthesized in GO solution and eventually Ce-MOF/GO nanocomposites are formed. In order to systematically investigate the influences of synthetic parameters on the morphology of Ce-MOF/GO nanocomposites, the morphologies of Ce-MOF/GO nanocomposites fabricated under different GO concentrations, $Ce(NO_3)_3$ concentrations, 1,3,5-BTC concentrations and reaction time are observed by SEM as shown in Fig. S3-S6 and they are described in detail in Supporting Information. Obviously, straw-sheaflike Ce-MOF are wrapped by graphene oxide and the size of Ce-MOF is uniform. Ce-MOF/GO nanocomposites after calcinations at 600 °C in Ar atmosphere and comminution are firstly characterized by FESEM and the results are exhibited in Fig. 1 (A) and (B). It is apparent that originally continuous GO nanosheets are destroyed and numerous nanoparticles exist due to the grinding effect. Fig. 1(C) curve c show the XRD pattern of Ce-MOF/GO nanocomposites after calcinations at 600 °C in Ar atmosphere, it is clearly observed that the diffraction peaks of samples are indexed to fluorite CeO_2 (JCPDS 34-0394) and rGO derived from Ce-MOF and GO, respectively, suggesting the formation of CeO_2/rGO nanocomposites. And this is in agreement with the SEM results in Fig. 1(A) and (B). In addition, the co-existence of CeO_2 and rGO is also confirmed by Raman spectrum analysis as shown in Fig. 1(D) curve c. One typical band near 460.6 cm^{-1} is attributed to CeO_2 F_{2g} mode[36], and typical D band (1348.1 cm^{-1}) and G band (1595.5 cm^{-1}) of rGO are clearly observed. Further investigation by TEM and HRTEM in Fig. 1(E) and (F) reveal that polycrystalline CeO_2 nanorods (nanoparticles) distribute randomly on the surface of rGO nanosheets. Furthermore, enlarged Raman spectra of Fig. 1(D) in Fig.S7 exhibit another two bands around 600.0 cm^{-1} and 250.2 cm^{-1} of Ce-MOF/GO nanocomposites after calcinations at 600 °C in Ar and 450 °C in Air belong to longitudinal optical mode due to oxygen vacancies [37] in CeO_2 and second-order transverse optical mode, indicating the formation of non-stoichiometric CeO_2 (denoted as CeO_{2-x}). As is known, the oxygen vacancies in CeO_2 plays significant role in improving their electrochemical properties and this will be discussed in detail later.

In order to further get insight into the phase transformation process of Ce-MOF/GO nanocomposites in different conditions, the morphologies and phases of Ce-MOF/GO nanocomposites after calcinations at 450 °C in Ar and Air atmosphere are studied and the results are presented in Fig. 1(C and D) and Fig. S8. Ce-MOF/GO nanocomposites could convert to CeO_2 completely after calcinations at 450 °C in Air. During this process, Ce-MOF decomposes into CeO_2 and GO is oxidized to CO_2, leading to the formation of light yellow powders, which is in line with XRD pattern in Fig. 1(C) curve a and Raman spectra in Fig. 1 (D) curve a, indicating the formation of phase pure CeO_2. However, no obvious diffraction peaks of CeO_2 are detected in Ce-MOF/GO nanocomposites after calcinations at 450 °C in Ar atmosphere, only two peaks ascribed to GO and rGO are observed. It is inferred that only part of GO converted to rGO and non-crystalline CeO_2 is formed in Ce-MOF/GO nanocomposites after calcinations at 450 °C in Ar atmosphere, which is in agreement with the results in Fig.1(D) and the TGA results in Fig. S1. In addition, SEM, EDX mapping and TEM images of Ce-MOF/GO nanocomposites after calcinations at 450 °C in Air and Ar atmosphere are exhibited in Fig. S8-S10, respectively. It is also confirmed that Ce-MOF/GO nanocomposites convert into phase pure CeO_2 and non-crystalline CeO_2/rGO/GO nanocomposites after calcinations at 450 °C in Air and Ar atmosphere.

X-ray photoelectron spectroscopy (XPS) is further employed to analyze the chemical bonding states of Ce-MOF/GO nanocomposites after calcinations at 600 °C in Ar and 450 °C in Air atmosphere, respectively. Fig. 2(a) demonstrates the XPS survey of Ce-MOF/GO nanocomposites after calcinations at 600 °C in Ar atmosphere and C, O and Ce elements are detected. Figs. 2(b-d) present the high resolution XPS spectra of C 1s, O 1s and Ce 3d, respectively. As shown in Fig. 2(b), high resolution

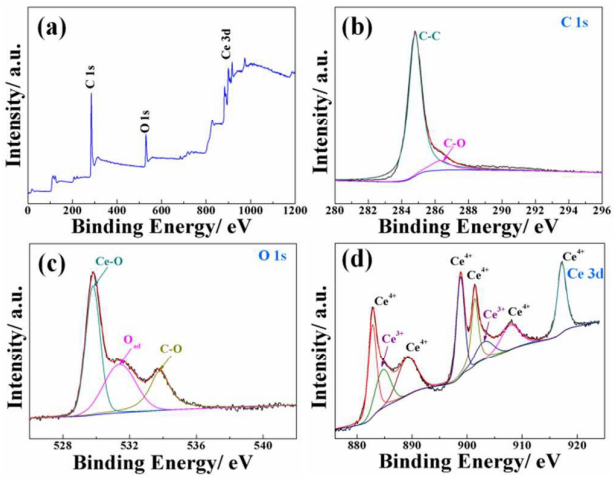

Fig. 2 (A) XPS survey spectra of CeO_{2-x}/C/rGO nanocomposites, (B) C 1s, (C) O 1s, (D) Ce 3d spectra of CeO_{2-x}/C/rGO nanocomposites

View Article Online
DOI: 10.1039/C7NR08858B

C 1s spectrum can be deconvoluted to two sub-peaks. The main peak centered at 284.8 eV is ascribed to C-C and another peak at 286.5 eV is attributed to C-O. And high resolution O 1s spectrum is deconvoluted to three sub-peaks as presented in Fig. 2(C), the peaks centered at 529.8 eV, 531.3 eV and 533.7 eV are attributed to lattice oxygen (Ce-O), adsorbed oxygen and C-O, respectively[38, 39]. The Ce 3d spectra in Fig.2 (d) is deconvoluted into four pairs of the spin-orbital doublet peaks ($3d_{5/2}$ and $3d_{3/2}$): 882.9 eV/901.4 eV, 885.1 eV/903.5 eV, 889.3 eV/908.1 eV and 898.9 eV/917.2 eV. Whereas the peaks located at 882.9 eV/901.4 eV, 889.3 eV/908.1 eV and 898.9 eV/917.2 eV belong to Ce^{4+} and the peaks at 885.1 eV/903.5 eV can be ascribed to Ce^{3+}. The presence of Ce^{3+} is due to the formation of oxygen vacancies in fluorite CeO_2 [40]. The fraction of Ce^{3+} species is evaluated by relative peak areas of Ce^{3+} according to previously reported work[38]. The calculated ratio of Ce^{3+} in Ce-MOF/GO nanocomposites after calcinations at 600 °C in Ar atmosphere is determined to be ca. 19.1%. Meanwhile, the ratio of Ce^{3+} in Ce-MOF/GO nanocomposites after calcinations at 450 °C in Air atmosphere is estimated to be 14.2%, which is presented in Fig. S11 and described in Supporting information.

According to the TGA results in Fig. S1, weight loss of Ce-MOF/GO nanocomposites treated in inert atmosphere is far less that of in Air. It is inferred that carbon is extensively remained except for rGO derived from GO, which is further confirmed by energy dispersive X-ray (EDX) spectroscopy equipped in TEM. As shown in Fig. 3, extensive

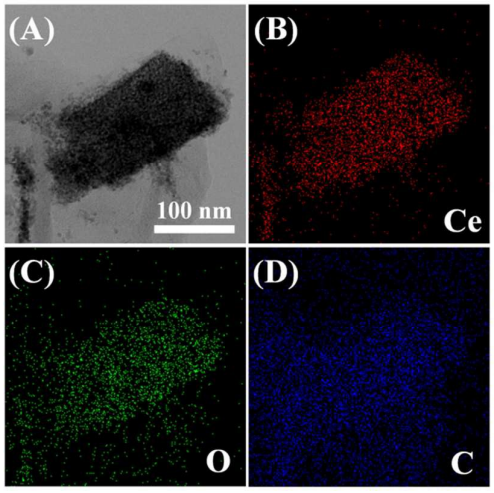

Fig. 3 (B-D) EDX mapping of (A) CeO_{2-x}/C/rGO nanocomposites

carbon is located in Ce-MOF derived CeO_{2-x} due to the decomposition of 1,3,5-BTC in inert atmosphere. Taking aforementioned analysis into account, CeO_{2-x}/C/rGO nanocomposites are eventually fabricated based on Ce-MOF/GO nanocomposites after calcinations at 600 °C in Ar atmosphere. In the control experiments, CeO_{2-x} nanorods and non-crystalline CeO_2/C/GO/rGO nanocomposites are also obtained based on Ce-MOF/GO nanocomposites after calcinations at 450 °C in Air and Ar atmosphere, respectively.

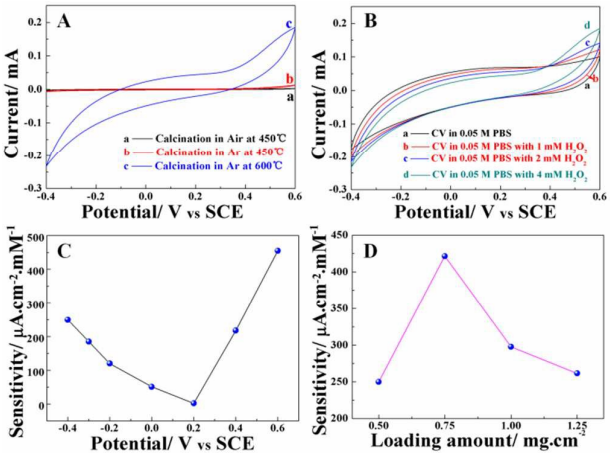

Fig. 4 (A) Cyclic voltammograms of Ce-MOF/GO nanocomposites calcinated at different temperatures in 0.05 M PBS with 4 mM H_2O_2, (B) Cyclic voltammograms of CeO_{2-x}/C/rGO nanocomposites in PBS with different H_2O_2 concentrations, (C) working potential and (D) loading amount optimization of CeO_{2-x}/C/rGO nanocomposites towards H_2O_2 detection

Prior to fabricating uric acid biosensor, electrochemical properties of as-prepared samples with different conditions are firstly investigated by cyclic voltammograms (CVs) and chronoamperometry towards detection of uricase catalyzed intermediates, H_2O_2. The sensing mechanism of uric acid biosensor is based on the detection of H_2O_2 concentration, which is eventually proportional to the concentration of uric acid. Fig. 4(A) shows CVs of Ce-MOF/GO nanocomposites calcinated at different temperatures and atmosphere in 0.05 M PBS with 4 mM H_2O_2. It is clearly observed that CeO_{2-x}/C/rGO nanocomposites exhibit higher catalytic properties towards H_2O_2 compared to that of CeO_{2-x} nanorods and non-crystalline CeO_2/C/GO/rGO nanocomposites. The reason for this phenomenon can be ascribed to the following aspects. One the one hand, higher concentration of oxygen vacancies in CeO_{2-x}/C/rGO nanocomposites favours the improvement of catalytic properties towards H_2O_2; on the other hand, good electrical conductivity of C embedded in CeO_{2-x} and rGO accelerates the electron transfer during electrochemical reactions.

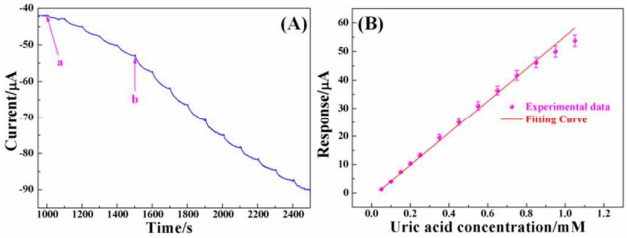

Fig. 5 (A) Amperometric responses of uric acid biosensor based on CeO_{2-x}/C/rGO nanocomposites with successive injection of uric acid with different concentrations. (a) 0.05 mM and (b) 0.1 mM, (B) Calibration curve of as-prepared uric acid biosensor.

View Article Online
DOI: 10.1039/C7NR08858B

In addition, cyclic voltammograms of CeO_{2-x}/C/rGO nanocomposites in 0.05 M PBS with different H_2O_2 concentrations are also carried out as presented in Fig. 4(B). Obviously, CeO_{2-x}/C/rGO nanocomposites exhibit oxidation and reduction capability towards H_2O_2 simultaneously due to Ce^{3+}/Ce^{4+} redox property in CeO_{2-x}. And anodic and cathodic currents increase with increasing of H_2O_2 concentrations. Fig. 4(C) depicts the working potential optimization of CeO_{2-x}/C/rGO nanocomposites towards H_2O_2 detection and the results are in line with CVs results in Fig. 4(B). Although the sensitivity of CeO_{2-x}/C/rGO nanocomposites towards H_2O_2 detection at 0.6 V *vs.* SCE is much higher than that working at negative potentials, negative potentials are preferred to be applied in uric acid biosensors by taking anti-interference ability into account. Eventually, -0.4 V is optimized and selected in the following experiments. As is known, loading amount of active materials plays a significant role in electrochemical properties. Therefore, influence of loading amount of CeO_{2-x}/C/rGO nanocomposites on the catalytic property towards H_2O_2 is studied as shown in Fig. 4(D). When the loading amount of CeO_{2-x}/C/rGO nanocomposites is lower, the catalytic property towards H_2O_2 detection is inferior. And its sensitivity of CeO_{2-x}/C/rGO nanocomposites towards H_2O_2 detection achieves the peak value with a loading amount of 0.75 mg cm^{-2}. If the loading amount is further increased, the sensitivities decrease as well due to slow mass transport and electron transfer. Therefore, loading amount of 0.75 mg cm^{-2} for CeO_{2-x}/C/rGO nanocomposites is optimized and utilized for the construction of uric acid biosensors.

In addition, calcinations temperature plays a key role in the performance of CeO_{2-x}/C/rGO nanocomposites towards H_2O_2 detection and it is investigated as shown in Fig. S12-S14 and Table S1. Obviously, CeO_{2-x}/C/rGO nanocomposites obtained after calcinations at 600 °C in Ar exhibited higher amperometric responses that those of CeO_{2-x}/C/rGO nanocomposites obtained after calcinations at 700 °C and 800 ℃ in Ar. Although the oxygen vacancies in CeO_{2-x}/C/rGO nanocomposites increased slightly when calcinations temperature increased to 700 °C and 800 °C, the catalytic performance of CeO_{2-x}/C/rGO nanocomposites towards H_2O_2 detection decreased. The reasons for this phenomenon are probably ascribed to the following aspects. On the one hand, oxygen vacancies in fluorite CeO_2 cannot increase proportionally with the increase of calcinations temperature because oxygen vacancies with supersaturation will result in the instability of CeO_2; on the other hand, aggregation of nanomaterials at higher calcinations temperature leads to the decrease the specific surface area, which reduces the active sites of CeO_{2-x}/C/rGO nanocomposites. Therefore, CeO_{2-x}/C/rGO nanocomposites obtained after calcinations at 600 ℃ in Ar are employed as substrate to construct uric acid biosensors.

Fig. 5(A) demonstrates typical amperometric responses of uric acid biosensor based on CeO_{2-x}/C/rGO nanocomposites with successive injection of uric acid with different concentrations. When uric acid is injected into PBS solution, it is catalyzed to H_2O_2, CO_2 and allantoin as it reaches the active sites of uricase[41]. Subsequently, the generated H_2O_2 is reduced by a great amount of Ce^{3+} in CeO_{2-x}, resulting in the formation of cathodic current as shown in Fig. 5(A). The amperometric responses of uric acid biosensor are eventually proportional to the injected uric acid concentration. The sensitivity of uric acid biosensors based on CeO_{2-x}/C/rGO nanocomposites is 284.5 $\mu A \cdot cm^{-2} \cdot mM^{-1}$, which is higher than those previously reported uric acid biosensors at low working potentials, such as PET and DTB on Au electrode (3.4 $\mu A \cdot cm^{-2} \cdot mM^{-1}$)[42], ZnO nanosheets (129.81 $\mu A \cdot cm^{-2} \cdot mM^{-1}$)[43], Thionine-SWNT (90 $\mu A \cdot cm^{-2} \cdot mM^{-1}$)[44], etc. The high sensitivity is probably ascribed to the extensive oxygen vacancies in CeO_{2-x} and fast electron transfer in carbon and rGO. Meanwhile, the large specific surface area (~93.7 m^2 g^{-1}, as shown in Fig. S12) of CeO_{2-x}/C/rGO nanocomposites is beneficial to adsorb much more uricase and improve the activity of enzymatic catalysis. The linear range between 49.8 and 1050.0 μM (R^2=0.995) is obtained according to the calibration curve of as-prepared uric acid biosensors as shown in Fig.5(B) and detection limit is calculated to be 2.0 μM based on Long's approach[45]. The performances of uric acid biosensors based on CeO_{2-x}/C/rGO nanocomposites were compared with those based on other substrates reported in the past decade and listed in Tables S2. Furthermore, uric acid biosensors based on CeO_{2-x}/C/rGO nanocomposites display excellent anti-interference ability towards ascorbic acid and urea coexisting with uric acid. This can be attributed to less negative working potential of as-prepared uric acid biosensors, avoiding the oxidation of ascorbic acid and urea at high working potentials.

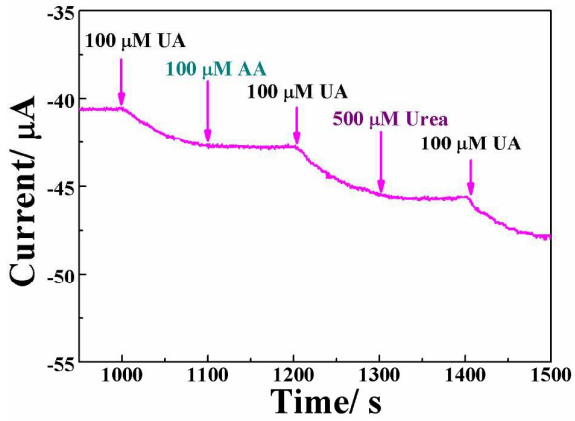

Fig. 6 Typical amperometric responses of CeO_{2-x}/C/rGO nanocomposites-based uric acid biosensor with injection of 100 μM UA, 100 μM AA and 500 μM urea.

Conclusions

CeO_{2-x}/C/rGO nanocomposites were designed and developed based on Ce-MOF in combination with graphene oxide. And CeO_{2-x}/C/rGO nanocomposites

View Article Online
DOI: 10.1039/C7NR08858B

were employed as novel substrate to construct uric acid biosensors. It was found that oxygen vacancies played a significant role in forming Ce^{3+} ions in CeO_{2-x}, which contributed to the superior electrocatalytic property towards H_2O_2 reduction and achieved the detection of uric acid at less negative working potentials. The biosensors presented a high sensitivity, wide linear range and low detection limit towards uric acid detection at -0.4 V *vs.* SCE. In addition, as-prepared biosensors based on CeO_{2-x}/C/rGO nanocomposites displayed excellent anti-interference ability towards ascorbic acid and urea coexisting with uric acid, which would allow the substrates to be employed in clinic applications.

Conflicts of interest

There are no conflicts to declare.

Acknowledgements

This work is financially supported by National Natural Science Foundation of China (Nos. 51402081, 51502071 and 51372063), AVIC Institute of Fundamental Technology Innovation Fund (Grant No. JCY2015A001) and Fundamental Research Funds for the Central Universities (Nos. JZ2016HGTB0719 and JZ2017HGTB0203).

Notes and references

1. J. Wang, Chem. Rev., 2008, 108, 814-825.
2. S. K. Arya, M. Datta, B. D. Malhotra, Biosens. Bioelectron., 2008, 23, 1083-1100.
3. K. Arora, M. Tomar, V. Gupta, Analyst, 2014, 39, 837-849.
4. J. W. Cui, E. E. Ogabiela, J. N. Hui, Y. Wang, Y. Zhang, L. Tong, J. F. Zhang, S. B. Adeloju, X. Y. Zhang, Y. C. Wu, J. Electrochem. Soc., 2015, 162, B62-B67.
5. B. Unnikrishnan, S. Palanisamy, S. M. Chen, Biosens. Bioelectron., 2013, 39, 70-75.
6. D. Y. Zhai, B. R. Liu, Y. Shi, L. J. Pan, Y. Q. Wang, W. B. Li, R. Zhang, G. H. Yu, ACS Nano, 2013, 7, 3540-3546.
7. R. J. Soto, B. J. Privett, M. H. Schoenfisch, Anal. Chem., 2014, 86, 7141-7149.
8. L. S. Wang, X. Gao, L. Y. Jin, Q. Wu, Z. C. Chen, X. F. Lin, Sens. Actuat. B-Chem., 2013, 176, 9-14.
9. M. B. Gholivand, M. Khodadadian, Biosens. Bioelectron.,2014, 53, 472-478.
10. S. Komathi, N. Muthuchamy, K-P. Lee, A-I Gopalan, Biosens. Bioelectron., 2016, 84, 64-71.
11. T. Ghosh, P. Sarkar, A. P. F. Turner, Bioelectrochem., 2015, 102, 1-9.
12. P. E. Erden, E. Kılıç, Talanta, 2013, 107, 312-323.
13. R. Ahmad, N. Tripathy, N. K. Jang, G. Khang, Y. B. Hahn, 2015, 206, 146-151.
14. M. Ahmad, C. F. Pan, Z. X. Luo, J. Zhu, J. Phys. Chem. C, 2010, 114, 9308-9313.
15. R. Sundar, C. R. Raj, J. Phys. Chem. C, 2010, 114, 21427-21433.
16. Y. L. Wang, Y. C. Zhu, J. L. Chen, Y. Zeng, Nanoscale, 2012, 4, 6025-6031.
17. J. W. Cui, S. B. Adeloju, Y. C. Wu, Anal. Chim. Acta, 2014, 809, 134-140.
18. S. K. Arya, S. Saha, J. E. Ramirez-Vick, V. Gupta, S. Bhansali, S. P. Singh, Anal. Chim. Acta, 2012, 737, 1-21.
19. A. Umar, R. Ahmad, S. W. Hwang, S. H. Kim, A. Al-Hajry, Y. B. Hahn, Electrochim. Acta, 2014, 135, 396-403.
20. Y. G. Liu, X. M. Zhang, D. N. He, F. Y. Ma, Q. Fu, Y. Hu, RSC Adv., 2016, 6, 18654-18661.
21. D. Patil, N. Q. Dung, H. Jung, S. Y. Ahn, D. M. Jang, D. Kim, Biosens. Bioelectron., 2012, 31, 176-181.
22. H. Y. Kim, H. M. Lee, G. Henkelman, J. Am. Chem. Soc., 2012, 134, 1560-1570.
23. C. W. Sun, H. Li, L. Q, Chen, Energy Enviorn. Sci., 2012, 5, 8475-8505.
24. T. Montini, M. Melchionna, M. Monai, P. Fornasiero, Chem. Rev., 2016, 116, 5897-6041.
25. A. A. Ansari, A. Kaushik, P. R. Solanki, B. D. Malhotra, Electrochem. Commun., 2008,10, 1246-1249.
26. M. H. Asif, S. M. U. Ali, O. Nur, M. Willander, C.Brännmark, P. Strålfors, U. H. Englund, F. Elinder, B. Danielsson, Biosens. Bioelectron., 2010, 25, 2205-2211.
27. N. Batra, M. Tomar, V. Gupta, Analyst, 2012, 137, 5854-5859
28. R. Ahmad, N. Tripathy, M. S. Ahn, Y. B. Hahn, Sci. Rep., 2017, 7, 46475(1-8).
29. H. C. Gao, H. W. Duan, Biosens. Bioelectron., 2015, 65, 404-419.
30. F. Xiao, Y. Q. Li, X. L. Zan, K. Liao, R. Xu, H. W. Duan, Adv. Funct. Mater., 2012, 22, 2487-2494.
31. Y. P. Ye, T. Kong, X. F. Yu, Y. K. Wu, K. Zhang, X. P. Wang, Talanta, 2012, 89, 417-421.
32. Y. Y. Shao, J. Wang, M. Engelhard, C. M. Wang, Y. H. Lin, J. Mater. Chem., 2010, 20, 743-748.
33. J. Chen, B. W. Yao, C. Li, G. Q. Shi, Carbon, 2013, 64, 225-229.
34. L. H. Jiang, M. G. Yao, B. Liu, Q. J. Li, R. Liu, H. Lv, S. C. Lu, C. Gong, B. Zou, T. Cui, B. B. Liu, G. Z. Hu, T. Wågberg, J. Phys. Chem. C, 2012, 116, 11741-11745.
35. S. Radhakrishnan and S. J. Kim, RSC Adv., 2015, 5, 12937-12943.
36. I. de C. Silva, F. A. Sigoli, I. O. Mazali, J. Phys. Chem. C, 2017, 121, 12928-12935.
37. M. Gao, J. Q. Lu, Y. N. Wu, Y. J. Wang, M. F. Luo, Langmuir, 2011, 27, 3872-3877.
38. X. T. Lin, S. J. Li, H. He, Z. Wu, J. L. Wu, L. M. Chen, D. Q. Ye, M. L. Fu, Appl. Catal. B: Environ. 2017, https://doi.org/10.1016/j.apcatb.2017.06.071.

View Article Online
DOI: 10.1039/C7NR08858B

39. D. Jampaiah, T. S. Reddy, A. E. Kandjani, P. R. Selvakannan, Y. M. Sabri, V. E. Coyle, R. Shukla, S.K. Bhargava, J. Mater. Chem. B, 2016, 4, 3874-3885.
40. A. D. Liyanage, S. D. Perera, K. Tan, Y. Chabal, K. J. Balkus Jr, ACS Catal., 2014,4, 577-584.
41. R. Devi, C. S. Pundir, Sens. Actuat. B: Chem., 2014, 193, 608-615.
42. S. Behera, C. R. Raj, Biosens. Bioelectron., 2007, 23, 556-561.
43. R. Ahmad, N. Tripathy, N. K. Jang, G. Khang, Y. B. Hahn, Sens. Actuat. B: Chem., 2015, 206, 146-151.
44. D. X. Chen, Q. Wang, J. Jin, P. Wu, H. Wang, S. Q. Yu, H. Zhang, C. X. Cai, Anal. Chem., 2010, 82, 2448-2455.
45. G. L. Long, J. D. Winefordner, Limit of detection: a closer look at the IUPAC definition, Anal. Chem., 1983, 55, 712A-724A.

View Article Online
DOI: 10.1039/C7NR08858B

Table of Contents

CeO_{2-x}/C/rGO nanocomposites were synthesized and utilized as platform to construct uric acid biosensors working at negative potential.